and Experimental Hall

A. Ferrari[*], K. Potter[+], S. Rollet[+] and P. R. Sala[*]

[*]INFN, Sez. di Milano, via Celoria 16, 20133 Milan, Italy
[+] CERN, 1211 Geneva 23, Switzerland

Abstract

This paper describes the calculations performed to characterise the radiation field in the ATLAS detector at the LHC and to design the shielding of the detector and experimental areas. After a short description of the ATLAS detector, the simulations made with the MC code FLUKA are described in some detail. The radiation fields calculated in the inner cavity, in the calorimeters, in the experimental cavern, in the shafts and an external skyshine region are presented. Different kinds of particles and thresholds are relevant in each of these regions and different quantities and available tools are needed to correctly characterise each case.

1 INTRODUCTION

ATLAS is a general purpose p–p experiment at the Large Hadron Collider (LHC), proposed by a collaboration of $\approx$1500 scientists representing $\approx$140 institutions in 31 different countries. The overall detector layout is shown in Fig. 1, as presented in the Technical Proposal [1] of December 1994.

The magnet configuration is based on an inner superconducting solenoid generating a 2 Tesla field in the inner detector cavity and large superconducting air-core toroids consisting of independent coils arranged with eight-fold symmetry outside the calorimetry. This concept results in a high-resolution, large-acceptance and robust stand-alone muon spectrometer with almost no constraints on calorimetry and inner detector. The air core toroid system, with a long barrel (5 m inner, 10 m outer radii and 26 m length) and two inserted end-cap magnets, generates a large field volume and strong bending power with a light and open structure. Multiple scattering effects are therefore minimal, and an excellent muon momentum resolution is achieved with three stations of high-precision tracking chambers. The muon spectrometer defines the overall dimensions of the detector. The outer chambers of the barrel are at a radius of about 11 m, and the third layer of the forward muon chambers is located at $\pm$ 21 m from the interaction point.

The inner detector is confined to a cylinder of length 6.80 m and radius 1.15 m in the field of the superconducting solenoid. Its structure is quite complex, being composed of several layers of Silicon, Transition Radiation Trackers (TRT) and GaAs detectors. We refer to [2] for details.

Electromagnetic calorimetry is performed by a Lead and liquid Argon (LAr) electromagnetic sampling calorimeter complemented by a LAr presampler. This is divided into a barrel, 6.3 m long extendending radially from 1.5 m to 1.98 m, and two end caps, covering the η range from 1.4 up to 3.2. The E.M. calorimeter has a mimimum thickness of 26.9 X_0. Hadronic calorimetry is performed by a barrel and two extended barrel iron and scintillator tile calorimeters, and by a Copper-liquid Argon calorimeter in the End Cap. The tile calorimeters have an inner radius of 2.28 m and an outer one of 3.88 m. Two $\approx$60 cm wide gaps (for cables, cooling, etc.) are present between the barrel (5.64 m long) and the two extended barrel (2.65 m long) sections. The end cap hadronic calorimeter covers the range $1.55 \leq |\eta| \leq 3.2$, and is 1.9 m thick (approximately 10 interaction lengths). Hermetic hadron calorimetry for jet and missing E_T measurements is extended from the central region into the forward regions by detectors covering the range $3.2 < |\eta| < \sim 4.9$. In the present ATLAS design these forward detectors are integrated into the end caps, sharing the same cryostat, at a distance of about 5 m from the interaction point. They are longitudinally divided into three modules, the first made of Copper (or Brass) and liquid Argon, the others of Tungsten and liquid Argon.

The overall weight of the ATLAS detector is 7000 tons.

For background calculations the experimental hall and the beam-related equipment must also be taken into consideration.

The ATLAS hall will be of oval cross-section, 48 m long, 26 m wide and more than 25 m high, with the beam pipe at a height of 11.3 m on average. This beam pipe is subdivided into different sections, with different diameters and materials. The layout is not yet final. A low-beta machine insertion, consist of quadrupole superconducting magnets, at the extreme ends of the hall extending into the tunnel. Two 2 m long cylindrical copper collimators will be installed in front of the quadrupoles to protect them from secondaries coming from the interaction point. They are planned to have an inner radius of 1.5 cm, corresponding to $|\eta| \approx 8$. These will be referred to in the following sections as "quadrupole collimators".

There are three major sources of radiation at the LHC: 1) particle production at the interaction point, 2) local beam losses, and 3) beam–gas interactions. The total beam loss around the ring should not exceed 10^7 protons s^{-1}, small compared to the p–p collision rate of $\sim 10^9$ s^{-1} per collision point. Beam–gas interactions are estimated to be $\sim 10^2$ m^{-1} s^{-1} in the interaction area. Therefore, the dominant radiation source will be from particles produced in proton–proton collisions at the interaction point. The enormous rate of these collisions makes radiation damage, activation of de-
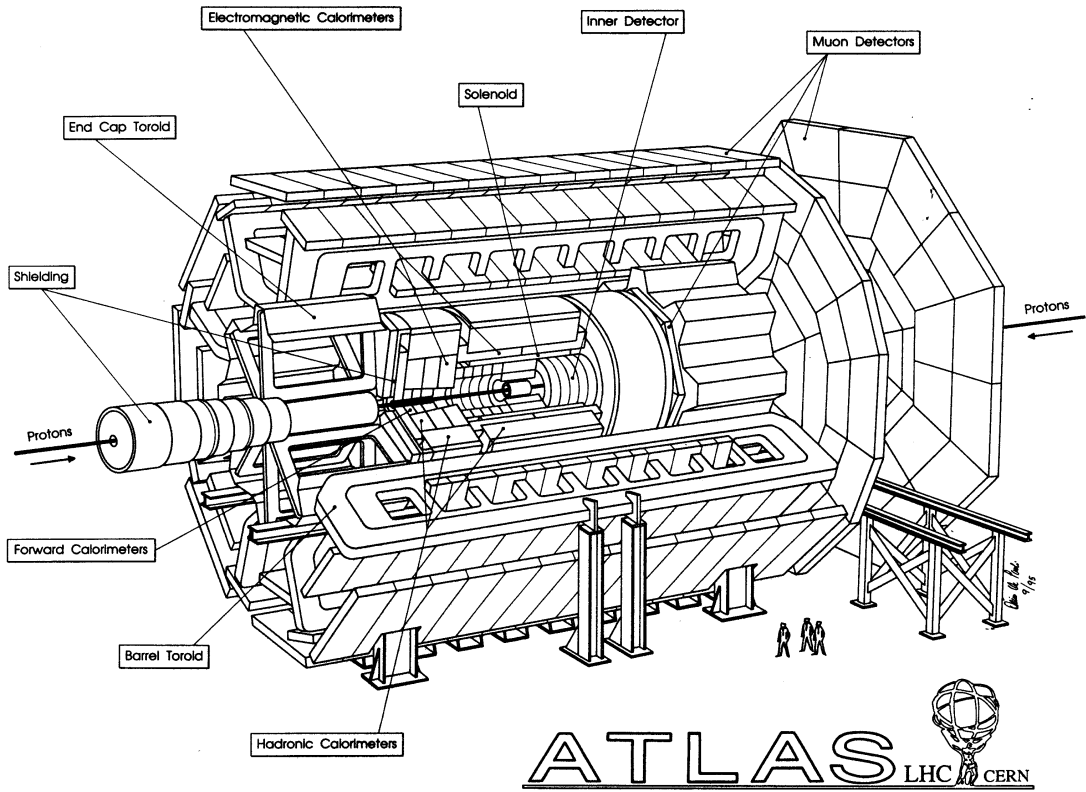
Figure 1: ATLAS layout

tector parts, and radiation-induced backgrounds in the detector a major concern.

Radiation backgrounds relevant for detector operation will be presented and discussed in section 3, while problems connected with personnel and environmental safety are presented in section 4. The tools used both in detector related and in environmental calculations are described in section 2.

Yearly integrated fluences reported in the following plots are normalized to an integrated luminosity of 10^5 pb^{-1} corresponding to 10^{34} cm^{-2} s^{-1} for 10^7 s at an event rate of $\approx 10^9$ s^{-1}, while whenever instantaneous values are presented, they are given for the nominal LHC luminosity of 10^{34} cm^{-2} s^{-1}. The cross section for inelastic p–p interactions at $\sqrt{s} = 14$ TeV has been assumed to be 80 mb in agreement with DTUJET predictions for all detector related calculations, and 100 mb to work with a conservative number for all radiation protection purposes.

2   SIMULATIONS

All detector simulations were carried out using the FLUKA code [3, 4, 5, 6], for transporting and showering the secondary particles generated in p–p events. This code has been extensively benchmarked against available experimental data over a wide energy range, for both hadronic and electromagnetic showers [7, 8, 9, 10, 11, 12]. In particular, the model used for hadronic interactions in the intermediate

energy range which is of utmost importance for all radiation related calculations, has been demonstrated to give fairly reasonable results, also when compared to the best available competitors [5, 13, 14].

The results presented in the following have been obtained using the most recent version of the DTUJET [15] event generator to produce the secondaries of the p–p events.

A few items of particular importance in the simulations carried out with FLUKA are discussed in detail in the following paragraphs.

Source   Whole events are sampled from a non-randomised collision file, including also diffractive events. The collision file was created out of 1300 events, with an average multiplicity of about 120 secondaries per event. The rapidity distribution of these minimum bias events has a plateau of 6.3 charged hadrons per unit of pseudorapidity at $\eta = 0$, including diffractive events. At the beginning of the calculations and at the end of each event, a new p–p collision is randomly selected among the recorded ones and its secondaries are banked in the simulation stack, to be showered through the whole geometry.

Geometry   The complex geometry of the ATLAS detector has been simulated in some detail using between 500 and 800 regions depending on the problem. A sketch of the geometrical layout used for the inner cavity and calorimeters, up to the first muon chambers, is shown in Fig. 2. All

the simulated dimensions are as close as possible to reality. Homogeneous materials have been used for some components, keeping the right proportion of constituents.
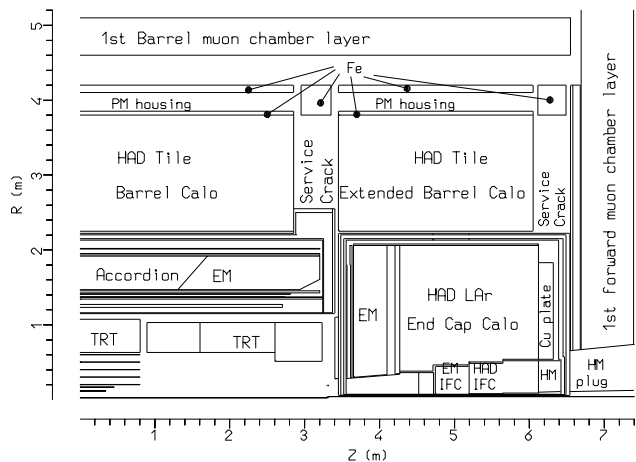

Figure 2: Inner and calorimeters regions of ATLAS geometry in FLUKA

Neutron cross sections An effort has been made whenever possible to use cross section data sets for neutron transport properly computed at the cryogenic temperature of some of the detector components. The temperature has indeed large effects on neutron cross sections both in the thermal and resonance regions.

Particle energy cut-off Particle transport thresholds have been set to 30 keV for photons, 0.5 MeV for electrons and 10 MeV for charged hadrons and muons, while neutrons have been followed down to thermal energies.

Biasing A major problem in these calculations is the huge amount of CPU time required to follow all secondaries of a 14 TeV event down to near-zero energy in such a complex geometry. Hence the powerful variety of variance reduction allowed by FLUKA is used to increase the speed and the statistical accuracy.

- Strong negative biasing using Russian Roulette at collision, weight windows and leading particle biasing for EM showers have been applied to medium-low energy particles in those components (Cu quadrupole collimator and forward calorimeters for example) where most of the energy is deposited, but that are embedded in massive shields. This avoided losing too much time fully showering the huge amount of low energy secondaries generated in these regions. This is very effective particularly for EM showers which are very CPU expensive and have little or no chance of escaping from the shield.

- Importance biasing and weight windows have been applied in such a way as to favour particles which are going in the "right" direction to escape into the hall (muon system), punching-through the calorimeters/shields or streaming through the detector cracks. Such particles, when reaching the outermost radii of the hall have undergone a progressive multiplication ("splitting") process with a factor of ≈ 500, therefore greatly improving the statistics in these regions where the attenuation factors are already large. Furthermore since the fraction of particles "physically" reaching the hall is small, the CPU penalty is acceptable and largely over-compensated by the reduction of errors due to statistics.

- Importance biasing together with a weight window is applied also in the lateral concrete wall of the hall in such a way as to compensate the exponential attenuation of particle fluence. In practice the wall is divided into 20 cm thick slices, and at each slice particles which are going deeper are "split" in such a way as to approximately compensate the exponential attenuation occuring in that slice (the applied splitting factor is 1.3). As a consequence the particle population and hence statistics are kept roughly constant throughout the wall, at the price of increasing linearly the CPU time with the wall thickness, rather than exponentially as would be required for an unbiased run aiming at the same statistics.

- Forced decay is applied everywhere to pions and kaons to enhance statistics for muon production. Indeed muons are so penetrating that even the small number produced by meson decays (dimensions are such that most mesons interact rather than decay) can eventually dominate the radiation environment at the largest thicknesses in the lateral direction.

Magnetic field A schematic magnetic field is included in the calculations. A perfect solenoidal 2 T field is assumed in the central cavity, while the Barrel Toroid field has been represented by an azimuthally symmetric toroidal field, with a radial behaviour and a peak value (≈ 1 T) consistent with the ϕ-averaged field of the actual toroid: rough fringe fields have been included. A uniform toroidal field of 1.4 T with no fringe field has been adopted for the forward toroid. The material of the forward toroid has been modeled in the calculations, including the eight-fold coils and the cryostat, since it represents a substantial amount of matter at the highest rapidity. No account has been taken of the Barrel Toroid material, since it represents a minor fraction of the total available space at the radial position where it sits.

CPU time The CPU time is of course strongly depending on the problem under investigation but with the strong biasing we have used typically we need between 3 and 7 minutes per event on a standard work-station IBM RISC6000 or DEC Alphastation. To reach a good statistical level for the plots presented later we used something between 800 and 1000 events.

3 RADIATION ENVIRONMENT FOR THE DETECTOR

Due to the huge LHC design luminosity, virtually no component of the detector can be considered unaffected by radiation. The problems associated are of different nature according to the considered subdetector and can be related to instantaneous rates (occupancy, pattern recognition, trigger) or to integrated ones (radiation damage, ageing, radioactivation).

While calorimeters are only sensitive to relatively large energy deposits, tracking chambers are also sensitive to low energy particles from shower tails and backsplash. The latter are mainly composed of neutrons, associated photons, and electrons. These particles contribute to the counting rate and to the radiation damage of the detectors. Radiation damage, however, comes mainly from energetic hadrons and total dose deposition, rather than from thermal energy neutrons and their associated photons. Activation is due to both spallation products from energetic hadrons, mainly in the shower bulk, and neutron capture. Detailed estimates of the radiation environment can be found in [16, 17] and references therein.

FLUKA and DTUJET have been extensively compared with experimental data [5, 10, 11, 14, 12, 15]; the overall uncertainty owing to minimum bias generation and showering should not be larger than 30%-40%.

Specific sources of additional uncertainty for background calculations for the muon system are discussed separately in the relevant paragraph.

Whenever isolevel maps are shown, full lines correspond to decades, long dashed lines to 1/3 of a decade and short dashed ones to 2/3 of a decade.

3.1 Radiation Environment in the Inner Detector

The inner detector is exposed to intense fluences of neutral and charged hadrons coming from particles produced directly in the p–p interactions and backscattered from the calorimeters. The total neutron fluence in the inner region can be considerably reduced by adding low-Z material close to the calorimeter walls. In the forward direction, 5 cm thick polyethylene layers are placed on the front faces of the endcap calorimeters, and 20 cm thick layers in front of the forward calorimeters. In the barrel section, at large angles, the low-z material of the polypropylene radiator of the Transition Radiation Tracker (TRT) fulfills most of the required shielding function.

Close to the interaction point, the particle flux is dominated by charged hadrons, which generate significant displacement damage in silicon and exhibit a typical $1/r^2$ dependence, where r is the distance from the beam axis and not from the interaction point, as shown in Fig. 3. Such a behaviour is expected for the fluence of particles generated at the interaction point with the expected flat $\frac{dN}{d\eta}$ distribution in the collision central region.

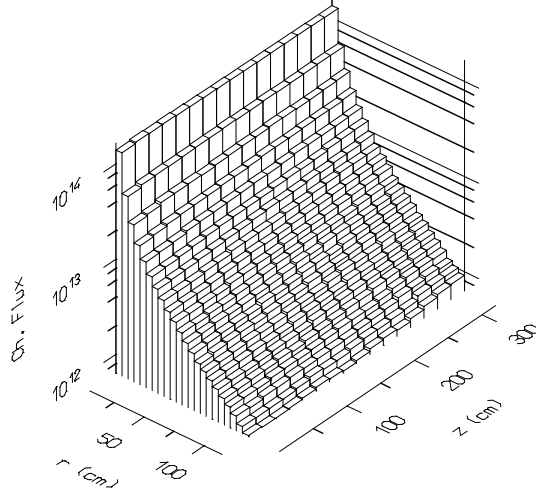The neutron fluence, mostly from albedo neutrons

Figure 3: Yearly integrated charged hadron fluence (cm^{-2} yr^{-1}) in the inner detector

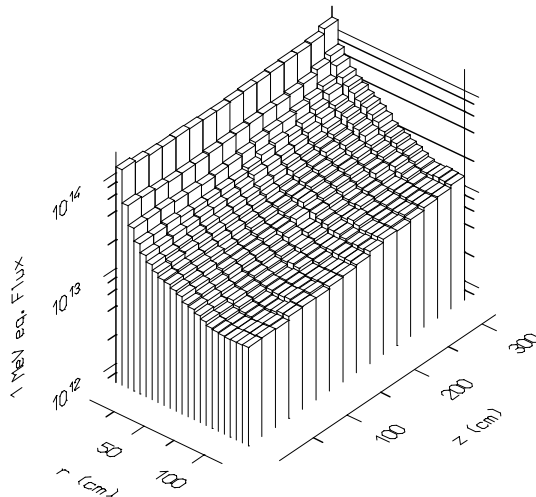Figure 4: Equivalent 1 MeV neutron fluence (cm^{-2} yr^{-1}) in the inner detector

backscattered from the calorimeters, is more uniform and dominates at larger radii (see Fig. 11). Damage to the silicon detectors can be estimated on the basis of fluences expressed as 1 MeV neutron equivalent. For this purpose we used the damage functions given in [18], supplemented with data from [19], for the lowest neutron energies. While the damage induced by neutrons with energies lower than 20 MeV is well understood, this is not true for charged pions, and, to a smaller extent, for protons which are the most abundant particles coming from the interaction point. The accuracy of the data for pions is of particular importance to the innermost Si layers, where the hadron fluence and hence the damage is dominated by secondary particles coming directly from pp events.

In Fig. 4 the neutron and charged hadron fluence expressed in 1 MeV neutron equivalent is shown.

Apart from damage, the huge background level in the central cavity raises severe problems of occupancy for the inner
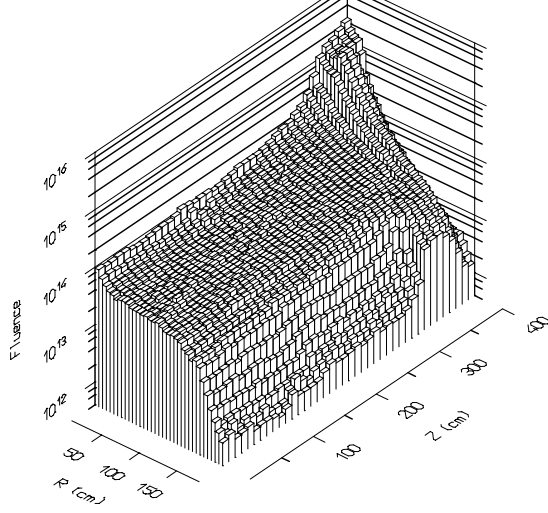
4

Figure 5: Yearly integrated photon fluence (cm^{-2} yr^{-1}) in the inner detector ($E_\gamma > 30$ keV). Points at $r < 10$ cm have not been plotted.

detector. In this respect, photons and associated electrons are also a source of trouble. The photon fluence in the inner cavity is shown in Fig. 5. As an example, the neutron and photon spectra in the barrel TRT position are shown in Figs. 6 and 7 respectively. The neutron spectrum is composed of a flat plateau typical of moderating materials, plus the evaporative peak in the few MeV zone and the quasi-elastic peak at higher energies. The photon spectrum helps in understanding the origin of the γ background: 95% of the spectrum is composed of photons with energy below 10 MeV, mainly coming from neutron capture. The 2.2 MeV peak from neutron capture on hydrogen can be clearly seen, as well as the annihilation peak at 511 keV. Only 5% of the spectrum is composed of high energy photons coming more or less directly from π^0 decays.
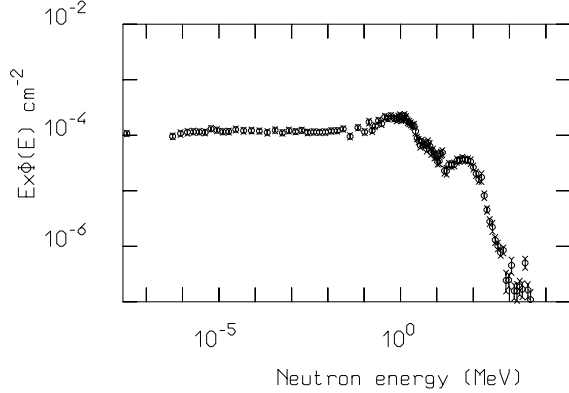

Figure 6: Neutron spectrum in the barrel TRT

3.2 Radiation levels in the Calorimeters

Most of the collision products are absorbed in the calorimeters, depositing relatively large amounts of energy, especially in the forward and end-cap e.m. calorimeter. The overall dose distribution in the inner detector and in the
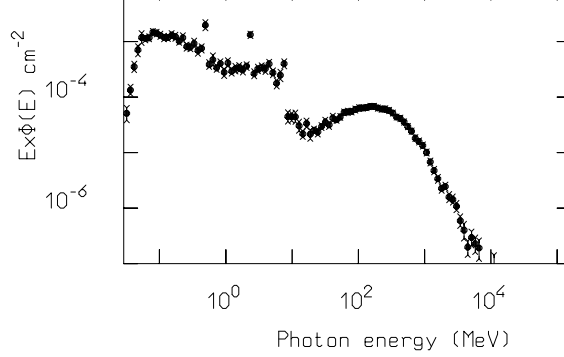

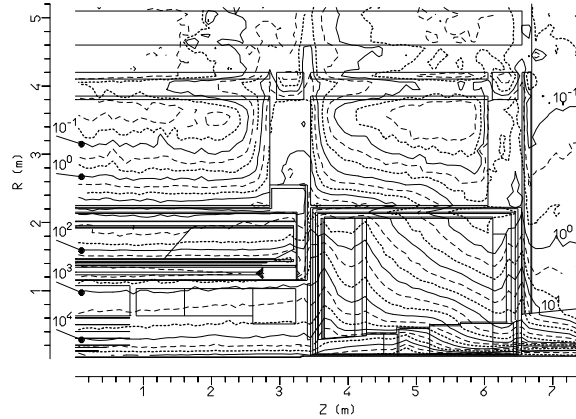Figure 7: Photon spectrum in the barrel TRT

Figure 8: Yearly integrated dose (Gy yr^{-1}) in the inner detector and the calorimeter system

calorimeter system is shown as a map in Fig. 8. The dose levels in the most exposed areas are shown in Fig. 9 for the EM calorimeters and in Fig. 10 for the Integrated Forward Calorimeter, as a function of the pseudorapidity η or of the
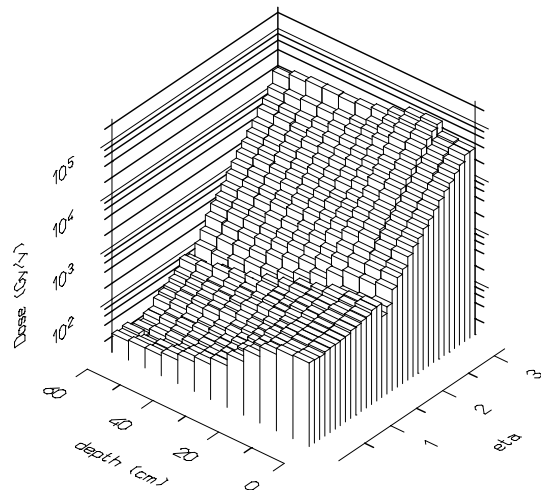

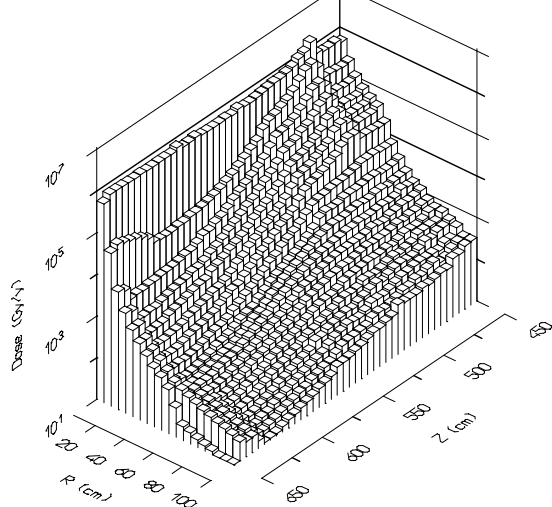Figure 9: Yearly integrated dose (Gy yr^{-1}) as a function of η and depth in the LAr EM calorimeters

5

Figure 10: Yearly integrated dose $(Gy\ yr^{-1})$ as a function of r and depth in the forward calorimeter region. Only points at $r > 5$cm have been plotted.
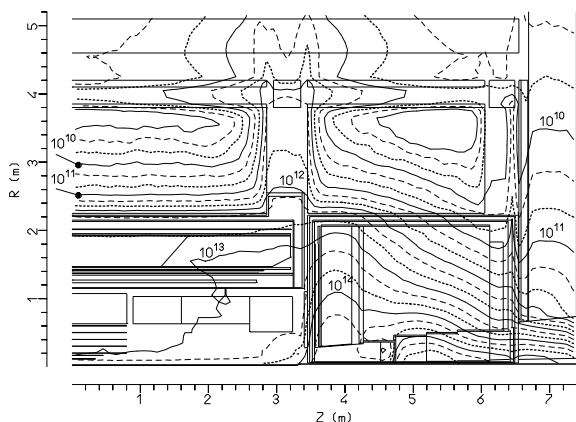

Figure 11: Yearly integrated neutron $(E_n > 100\ keV)$ fluence $(cm^{-2}\ yr^{-1})$ in the inner detector and the calorimeter system

radius r, and of the depth in the calorimeters. The dose distribution in the EM calorimeters decreases rapidly with increasing depth, showing that it is dominated by electromagnetic showers, coming in turn from π^0's. The increase with η is dramatic, and makes the Integrated Forward Calorimeter a very hot region. The neutron fluences in the central cavity and in the calorimeters are shown in the map in fig.11. Only neutrons with $E > 100$keV are included. The fluences in the Integrated Forward and on the front of the EM calorimeters are relevant from the point of view of the radiation resistance of electronics and materials. The situation at the level of the tile calorimeters is much better, both for dose and for neutron fluence, such as to allow the use of scintillation detectors. The service cracks act as chimneys, and within them radiation levels are substantially higher than in the surrounding tile calorimeters.

3.3 Shielding Strategy for the Muon System

While the background in the inner detector and in the calorimeters cannot be substantially shielded without spoiling the detectors themselves, the background in the muon chambers and in the experimental hall can be reduced by large factors by adding appropriate shielding, surrounding the radiation sources hermetically as possible. Extensive efforts have been aimed at optimising this shielding in different parts of the detector [16].

Including the forward calorimeters, integrated into the end caps, the calorimeters provide an almost hermetic shielding up to $\eta = 4.9$. The copper collimators for the low beta quadrupoles act as backstops. Only two well localised sources of background remain, besides punchthrough from the calorimeters: the inner edges of the end-cap calorimeter cryostats and the collimators.

These sources are surrounded by a composite shield. Its inner edge is projective and follows the $\eta = 4.6$ line, staying in the shadow of the forward calorimeter. The innermost layer of the shielding acts as a hadron shield, it should have a short hadronic interaction length, but should not increase the low-energy component of the neutron spectrum which is effectively moderated and eventually captured through elastic scattering and radiative capture on hydrogen. A layer of 33 cm of polyethylene has been placed inside the cold volume of the end-cap toroids (encapsulated in stainless steel boxes). The shield behind the end-cap toroids, up to the end of the hall, is surrounded by a 15 cm thick polyethylene layer, and an additional layer of 5 cm of lead, to shield against photons from neutron capture. The outer edge of the lead layer follows the $\eta = 3$ line.

A sketch of the geometry implemented in FLUKA for the calculations presented in the Technical Proposal is shown in Fig. 12.
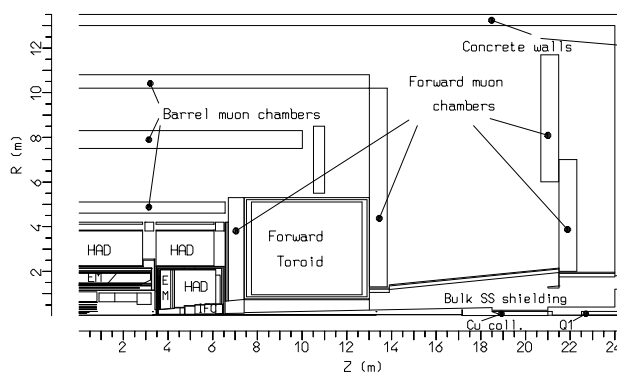

Figure 12: ATLAS geometry in FLUKA

The map of neutron fluence in the hall for the "starting point" with no shielding and an old configuration of the detector is presented in Fig. 13. It must be stressed that such a map does not contain the contribution of punchthrough particles which was computed separately. Only particles escap-
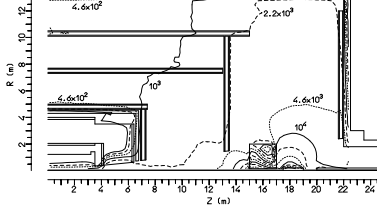
Figure 13: Neutron (thermal ones included) background fluence rate (kHz/cm^2) in an old configuration

ing through the End Cap inner bore into the hall and interacting in the hall itself, mainly in the Forward calorimeters (placed at some 15 m from the interaction point at that time) and in the quadrupole collimator have been taken into account. From a first look at the flux distribution for this unshielded geometry, it is evident that the main background source is the collimator. Starting from this point various shielding schemes have been tested, and a lot of work has been done trying to optimise the shielding strategy and the detector configuration with respect to background.

The resulting fluxes in the Technical Proposal configuration for neutrons and photons, presented in Fig. 14,16 now inclusive of punchthrough particles, show in an exhaustive manner the efficiency of the shielding around the collimator and quadrupoles. Despite the tremendous amount of energy deposited in such components their influence on the total background rate is now small.
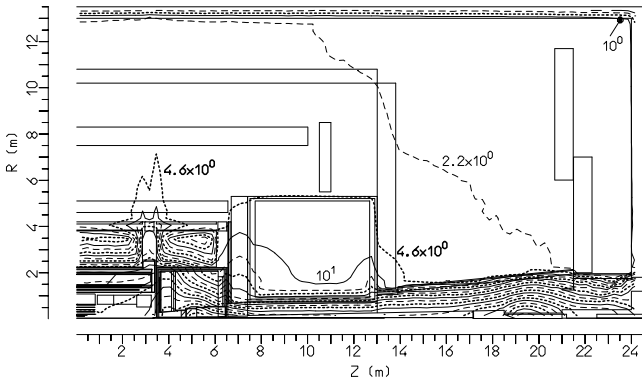

Figure 14: Neutron (thermal ones included) background fluence rate (kHz/cm^2) in the Technical Proposal shielding configuration

The residual background rate, is dominated by particles leaking from the region of the Forward Toroid, where the shield outer radius is limited by the cryostat, and the inner one is limited by the danger of intercepting particles not shadowed by the calorimeters [17]. The gaps at the end of the barrel and extended barrel tile calorimeters, where the electronics of the LAr calorimeters will be placed, are critical locations. Even with the presence of an iron plug, covering 60% of the hole, the streaming through the gaps is im-

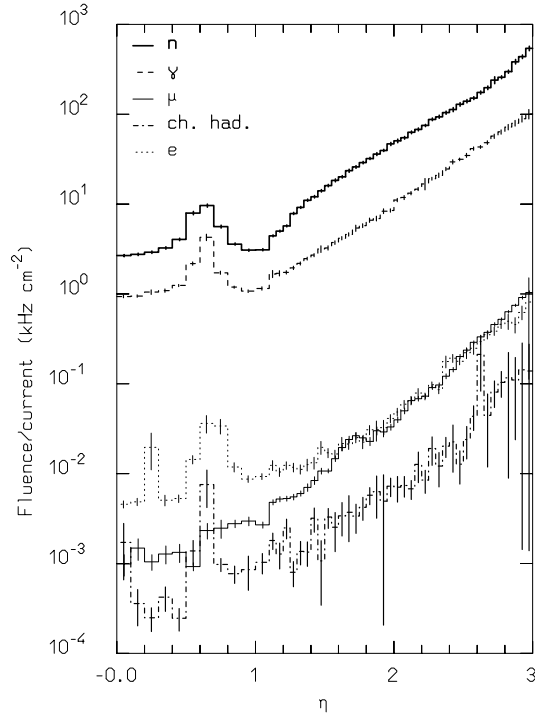portant and affects the background in the external regions.

Figure 15: Total background in the first muon station as a function of pseudorapidity; fluence rates are shown for neutral particles, current rates for charged particles.

Despite the large reduction factors achieved, the background levels, shown as a function of η in Fig.15, are just acceptable from the point of view of safe operation of the muon tracking and trigger chambers.

In order to estimate the relative impact of the various background components on muon chamber occupancy, the chamber efficiencies should be taken into account. The order of magnitude of muon chamber sensitivities is about 1% for photons and 0.1% for neutrons[20], while it is almost unity for charged particles.

In Fig.15 the effect of the cracks is evident, together with the strong increase of charged particle fluences at the highest rapidities. Among these, muons are very difficult to reduce. The hardness of their spectrum renders unaffordable any reduction strategy based on a plain thickening of the calorimeters and/or shielding plates and plugs. A simple simulation showed that the expected reduction is of the order of 1% per extra cm of Copper. A careful inspection of the results shows indeed that the background in the first muon station is punchthrough dominated for the last 0.7 units of rapidity.

A discussion of the impact of neutral and charged particle backgrounds on the muon system operation is outside the aims of this paper (details can be found in [1, 20]). However, it must be stressed that for most of the muon chamber surfaces but not the inner forward station at the highest rapidities, the hit rate is dominated by photon interactions. Taking

into account that most of the photon fluence does not come from punchthrough but is generated by neutron interactions all around the hall, it is clear that the accuracy of our predictions relies heavily on the full chain of processes going from energetic particles to hadron showers and to MeV neutrons, which are scattered, moderated and eventually captured.

Therefore several extra factors contribute to the uncertainties of the background estimates in the muon chambers:
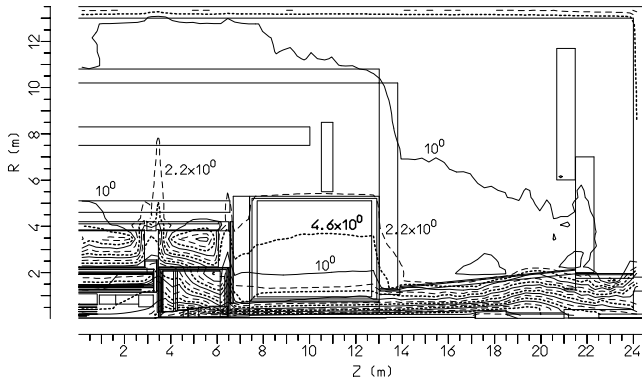

Figure 16: Photon (E_{ph} > 30 keV) background fluence rate (kHz/cm^2) in the Technical Proposal shielding configuration

- **Shielding hermeticity:** The proposed shielding is very effective provided cracks and openings can be kept well below 1% of the total solid angle. An overall 1% aperture would result in at least a factor two higher backgrounds. Similar effects could originate from even smaller cracks, if located close to the main sources of background. Therefore, care must be taken to make the final shielding at least as effective as in the present design.

- **Material composition:** Most of the background in the hall comes from neutrons and their capture photons. Neutron cross-sections, particularly in the thermal region where most of the captures occur, are very different from one isotope to another, with variations as large as four orders of magnitude. As a consequence, the material composition must be known to better than 10^{-3}. Of course this is not possible at the present design stage and will always be difficult. The resulting uncertainty is not easy to estimate, but should be less than 30% provided care is taken with those few isotopes having very large capture cross-sections.

- **Induced radioactivity:** An additional contribution to the background comes from photons emitted following radioactive decays of isotopes in the hall. All isotopes with a half-life shorter than several months, which are the vast majority, will eventually come into equilibrium and their decay rate will be equal to the production rate. Therefore, neglecting stable

isotopes, each nonelastic interaction or capture is an extra source of typically a few MeV of β^-, β^+ and/or photons. A quantitative estimate is difficult, however, we expect that this contribution will be less than 20–30%.

- **Neutron cross-sections:** Neutron cross-sections are well known for many, but not all, isotopes. Furthermore the accuracy of the photon production data (for many isotopes they have never been measured) is usually worse than that of the neutron scattering cross-sections. As the detector is mostly sensitive to capture photons, an overall uncertainty of 40% from this source alone should be assumed.

Combining these errors, an overall uncertainty of at least a factor two should be assumed for the background in the muon system.

4 PERSONNEL AND ENVIRONMENTAL SHIELDING

A huge underground experimental cavern must accommodate the ATLAS detector and allow simple and convenient installation and maintenance procedures for the whole lifetime of the experiment. The trigger and readout electronics must be located within the shortest possible distance from the detector and be permanently accessible. They must be housed in a separate cavern connected with the main cave with different kinds of passages both for cables and personnel. Two big vertical shafts connect the experimental cave with the surface, 80 m above. The size and shape of these shafts are determined by the dimensions of the coils of the barrel toroid and the end-cap toroids which have to be lowered into the cavern in one piece. The layout of all these concrete underground constructions is given in Fig. 17.

A realistic experimental hall with a lateral flat wall between the main cavern and the side electronics room and with two vertical shafts is implemented in FLUKA to simulate the radiation field in the hall and along and outside the shafts. The complete detector geometry previously described is inserted in this hall. The relevant geometry description implemented in FLUKA is presented in Fig. 18. The left figure represents a cross section in the zy plane showing both of the vertical shafts, while the right one is a cut through the xy plane in the centre of the largest one.

In order to decide the thickness of the concrete wall of the main cave, required to reduce the dose in the lateral equipment cavern below the 10 μSv/h allowed for a controlled area, the total dose equivalent rate inside the lateral wall has been computed.

A preliminary study has been made to analyse the different kinds of particles present in the wall. In Fig. 19, the fluence rate of neutrons, photons, muons and charged hadrons, are presented versus depth inside the concrete wall. These fluences are scored inside the wall with a binning granularity of 20×50 cm using a track-length estimator, but in these figures only the average over the whole wall length is presented. For the first half of the wall the dominant radiation
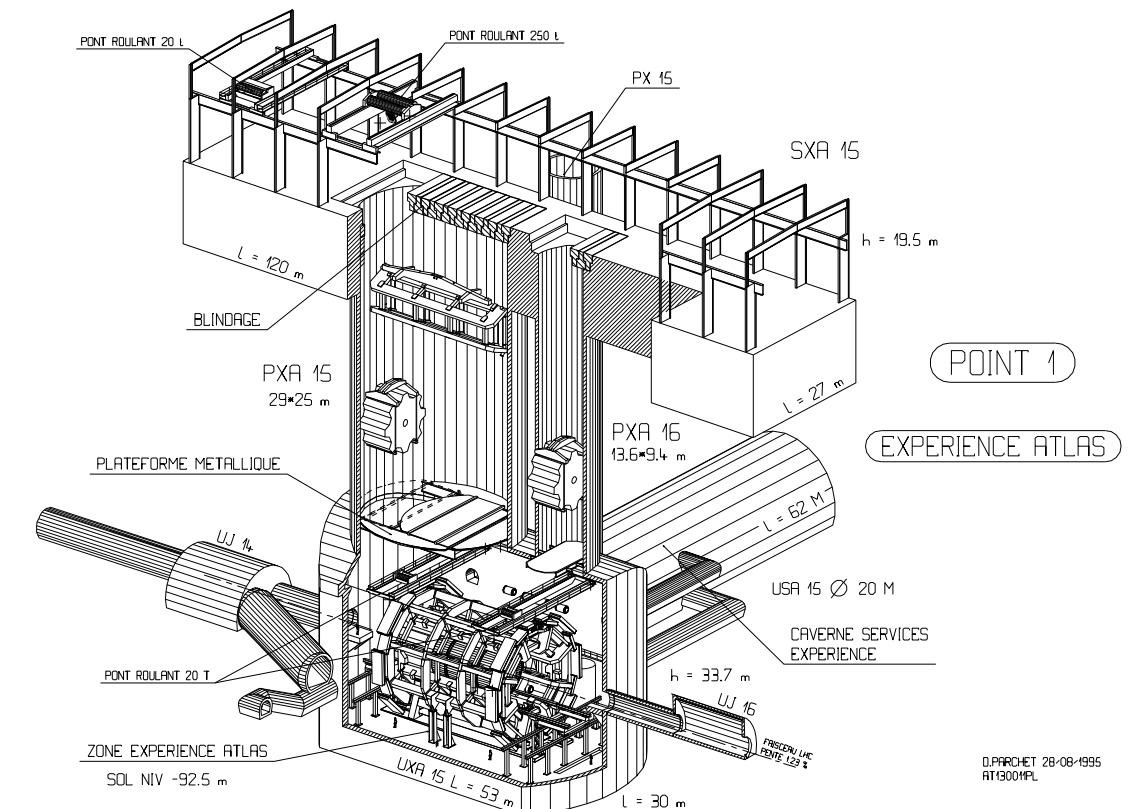
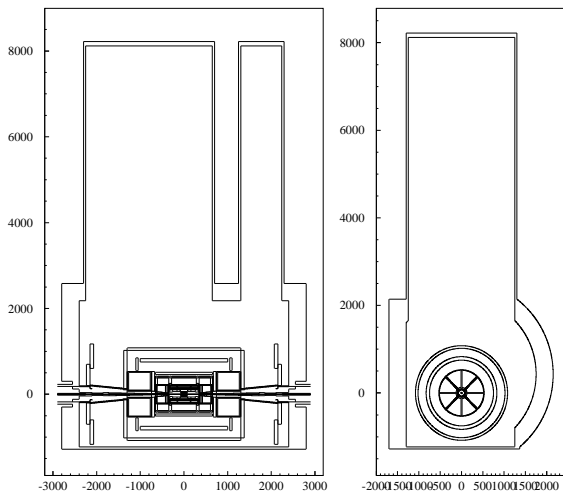Figure 17: ATLAS assembly and buildings at LHC point 1

Figure 18: Sketch of the ATLAS geometry simulated in FLUKA code. Cut through the zy plane (left) and through the xy plane (right).

components are neutrons and photons. It is interesting to note, however, that after 2–3 m of concrete the muon contribution becomes inportant. From the same figure it is also evident that up to 3 m, the photon and charged hadron flu-

ences are in equilibrium with the neutron one as expected, since all exhibit the same exponential attenuation. There is clearly an initial higher slope, due to soft neutrons and photons which are very abundant in the hall due to multiple reflections and that are rapidly attenuated in the wall. It is also interesting to note how the photon fluence starts to decouple from the neutron one around 3 m where the muon component is no longer negligible. This is due to muon interactions, (mostly δ ray production, bremsstrahlung and pair production for the most energetic), which contribute to the photon fluence.

Using a boundary crossing estimator, both fluences and spectra of the particles inside the concrete wall are scored at different positions. From these fluences, the corresponding dose equivalent, due the different particles, obtained by folding the scored spectra with suitable conversion factors [22] are plotted in Fig. 20. While the dose equivalent due to neutrons is the most important, in the last metre of the concrete the muon component starts to dominate.

The neutron spectra at the same positions, inside the concrete wall, are presented in Fig. 21, from which, aside the pronounced peak at higher energy, it is possible to see the importance of the low-energy component.

The total dose equivalent obtained summing all the contributions due to the different kinds of particles is then presented in Fig. 22 using the cross symbols. In the same figure, the total dose equivalent obtained from the energy density scoring provided by FLUKA, in which the deposited energy
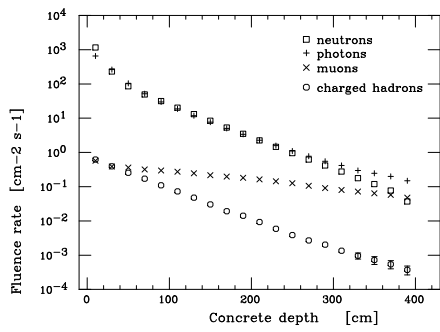
9

Figure 19: The fluence rate of different particles, averaged over the whole wall length, versus depth inside the concrete wall. The error bars (due to statistical error only) are smaller than the symbols almost everywhere.

due to all processes is given directly as GeV cm^{-3} per unit primary particle weight and applying a reasonable average quality factor Q = 5 is represented by open circles. Finally the hadronic star density computed with a threshold energy of 50 MeV and multiplied by a conversion factor of 4.5×10^{-8} Sv cm^3/star [23] is also shown, for comparison.

The agreement between the three methods used to estimate the total dose is reasonable for the first 2 m of concrete, while the dose at the largest depth computed by the energy deposition is overestimated due to the adopted quality factor. The partial doses also indicate that the slowly decreasing tail at the largest depths is due to muons.
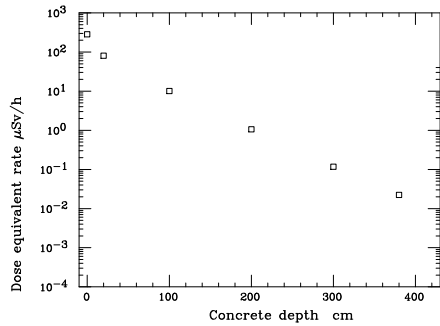

Figure 20: The separate dose equivalent rate due to neutrons, photons, muons and charged hadrons, averaged over the whole wall length, versus the concrete depth.

Fitting the results shown in Fig. 22 with three exponential curves, the resulting attenuation lengths are 50 g cm^{-2} ($\approx$20 cm for our concrete density: ρ=2.42 g cm^{-3}) for the initial slope, 100 g cm^{-2} ($\approx$40 cm) for the second one and 300 g cm^{-2} ($\approx$125 cm) for the last layers. The first value, concerning an initial region of some cm, is due to the quick absorbtion of the soft part of the neutron and photon spec-

trum. The second one, in the central part of the wall, is consistent with the typical attenuation length of hadronic cascades in the lateral direction and is mainly determined by the attenuation of neutrons in the few hundreds MeV range (where the interaction cross section is at minimum) which are well known as the particles propagating cascades beyond the shower maximum. It is worthwhile to stress that these neutrons, while ruling the cascade propagation, do not necessarily represent the largest source of dose equivalent, which is usually mainly due to neutrons in the MeV region, which are in equilibrium with the fast component of the cascade. The latter value for the attenuation length is in naive agreement with the expectations for a decay muon component.

More details on the attenuation of dose equivalent rate inside the concrete wall could be found in Ref. [21].
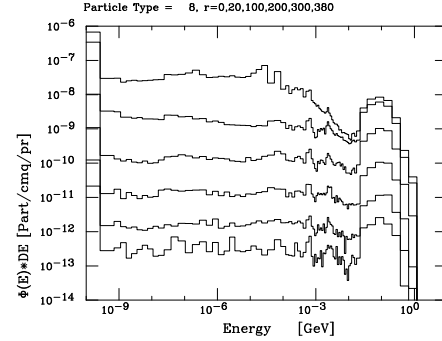

Figure 21: The neutron spectra at different depths (0, 20, 100, 200, 300, 380 cm) inside the concrete wall.

The variation of the dose equivalent inside the wall in the z direction is not very pronounced but the presence of weak points in the internal detector shielding is noticeable in the region at the beam level [25]. More variation is found considering positions at different heights from the floor.

For that reason the vertical wall has been divided into three horizontal strips along the complete length of the hall; each strip is 9.5 m high. The lowest one, starting from the floor (y=1), a central one at the beam level (y=2) and an upper one up to the ceiling (y=3). As expected, the maximum dose rate versus the distance from the beam axis, inside the concrete wall, occurs in the central region, since it is the closest to the beam, as shown in Fig. 23, while the average over the whole wall is lower than this maximum by about a factor of two.

Considering the variation of the dose distribution with position and the different spectra of the particles, two metres of concrete are enough to shield safely the control room, taking a reasonable safety factor into account.

A detailed analysis of particle fluences up the two large access shafts was also made with FLUKA to determine the correct thickness for the shielding plugs at the top. The overall attenuation factor is fairly large: the fluence of neutrons, which is the most important component of the parti-
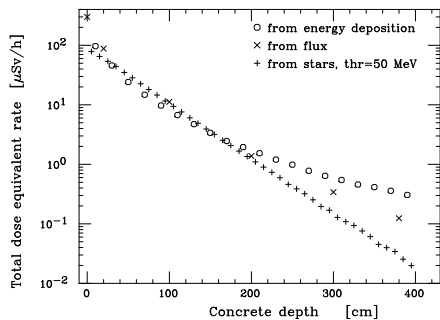
Figure 22: Total dose equivalent rate, averaged over the whole hall length, versus the concrete depth for different kinds of dose estimators.

cles streaming in this region, changes by nine orders of magnitude between the central region of the detector, at the beam level, and the top of the shaft. The neutron energy spectrum also changes from the bottom to the top of the shaft because of the attenuation due to air, as shown in Fig. 24.
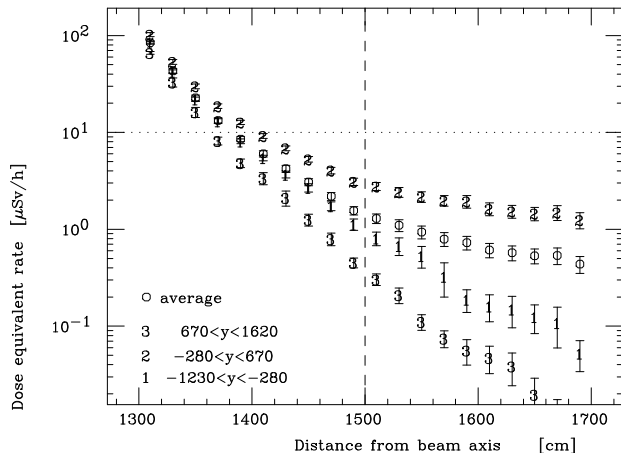

Figure 23: Dose equivalent rate, averaged over the whole wall length, versus the distance from the beam line. Together with the average over the wall height the different contributions coming from the three different vertical regions are plotted. The first surface of the concrete wall is at 1300 cm, the dashed line is at 200 cm depth.

Semi-analytical methods based on experimental results and detailed simulations, have been developed [24] in order to evaluate the attenuation of particle streaming through multi–legged mazes. "Universal" curves which give the attenuation factor of each maze leg as a function of the leg length in units of the square root of the cross sectional area can be used for these purposes. However, since the dimensions of the shafts are quite large, it is difficult to establish the correct normalisation and therefore the universal curve
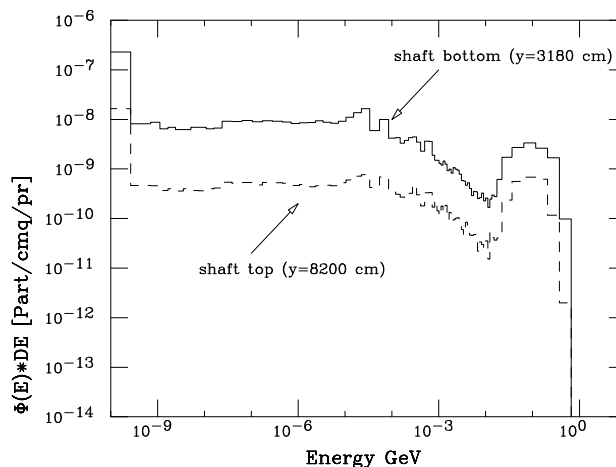

Figure 24: Neutron spectrum at the bottom and at the top of the larger shaft.

cannot be easily applied in this case. The universal curve is a reasonable approximation to the attenuation along the shafts, even though it appears that the attenuation along the largest one is indeed somewhat steeper than predicted by the universal curve [25].

The computed dose equivalent at the top of the shafts is higher than the permissible level for the personnel working in the surface buildings. Therefore the best way to shield this radiation was investigated considering different thicknesses of concrete for the top plug.

The resulting neutron dose equivalent on the external surface with an 80 cm concrete plug at the top of the big shaft and a 40 cm for the small one, is presented in Fig. 25, in a cylindrical region of 100 m height and 100 m radius. From this figure it is possible to appreciate that with such a thickness the dose where the surface buildings will be located is below the 1 μSv/h level allowed for a surveyed area and substantially below 0.1 μSv/h at the site fence (100 m away). Taking into account a safety factor and the uncertainties related to the complexity of the problem and to the large fluence attenuation, the final thickness of the plugs should be 120 cm of concrete equivalent for the big one and 80 cm for the smaller one. These thicknesses are expected to be adequate for the ultimate LHC performance which will only be achieved after many years, if at all.

5   CONCLUSIONS

A detailed model of the ATLAS detector has been implemented in the FLUKA MC code, accounting for transport and showering of the secondary particles created at the interaction point. These have been generated through the DTU-JET minimum bias code. This allowed the determination of the characteristics of the radiation field in different parts of the detector and to evaluate the dose and fluence level to which the electronics and subdetectors will be exposed. From yearly integrated quantities, like dose rate and neu-
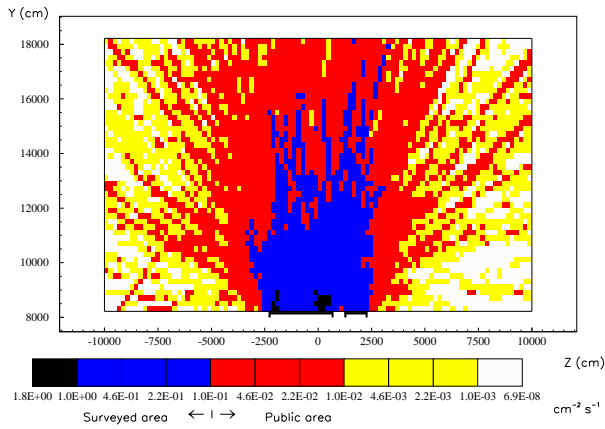
Figure 25: Dose equivalent rate (μ Sv/h) on the external surface with concrete plugs (80 cm for the big shaft and 40 cm for the small one).

tron (or neutron equivalent) fluences, the radiation damage and detector ageing can be evaluated in the different ATLAS subdetectors. From instantaneous fluence rates or currents an estimate of detector occupancy can be made.

The latter point is important mainly in the muon system, where, however, there are more possibilities of action: after having determined the main sources of background, a careful study of the shielding around these sources has been performed, and succeeded in reducing strongly the background.

Our calculational method is sufficiently accurate to yield a quantitative determination of the thickness of the concrete shield required in order to reduce the dose equivalent rate below the relevant limits in different locations around the detector.

In particular, the resulting thickness of the lateral wall must be equivalent to 2 m of concrete in order to achieve a reduction of the dose equivalent rate in the control room below the allowed limit of 10 μSv/h. The computed minimum thicknesses for the top plugs of the shafts are of 120 cm and 80 cm for the large and small shaft, respectively, having taken a reasonable safety factor into account.

Thanks to these two plugs, the dose level in the surface building will be reduced substantially below the level of 1 μSv/h, allowed for a surveyed area. The dose at the fence will in turn be below 0.1 μSv/h, as required for a public area, even at the ultimate level of LHC performance.

Acknowledgments

We would like to warmly thank A. Fassò for all his help.

6   REFERENCES

[1] ATLAS Collaboration, *Technical Proposal for a General Purpose pp Experiment at the Large Hadron Collider at CERN*, CERN/LHCC/94-43 (1994).

[2] J. Baines et al., ATLAS internal note INDET-No-66 (1994)

[3] A. Fassò et al, Proc. of the workshop on Simulating Accelerator Radiation Environment, SARE, Santa Fe, 11-15 January (1993), A. Palounek ed., Los Alamos LA-12835-C 1994, (p. 134).

[4] A. Fassò, A. Ferrari, J. Ranft, and P.R. Sala, Proc. of the IV Int. Conf. on Calorimetry in High Energy Physics, La Biodola, (Elba), A. Menzione and A. Scribano eds., World Scientific, p. 493 (1994).

[5] A. Fassò, A. Ferrari, J. Ranft, and P. R. Sala, Proc. of the "Specialists' Meeting on Shielding Aspects of Accelerators, Targets & Irradiation Facilities", Arlington, April 28-29 1994, published by OECD/NEA (1995), 287.

[6] A. Fassò, A. Ferrari, J. Ranft, and P. R. Sala, *An update about FLUKA*, Proceedings of this Conference.

[7] A. Ferrari, P. R. Sala, G. Guaraldi and F. Padoani, Nucl. Instr. Meth. **B71** (1992) 412.

[8] P. A. Aarnio et al., Proc. of the MC93 Int. Conf. on Monte Carlo Simulation in High-Energy and Nuclear Physics, Feb. 22-26, 1993, Ed. P. Dragovitsch, S.L. Linn, M. Burbank, World Scientific, Singapore, 1994 (p. 100).

[9] P. A. Aarnio et al., Proc. of the MC93 Int. Conf. on Monte Carlo Simulation in High-Energy and Nuclear Physics, Feb. 22-26, 1993, Ed. P. Dragovitsch, S.L. Linn, M. Burbank, World Scientific, Singapore, 1994 (p. 88).

[10] A. Fassò, A. Ferrari, J. Ranft, P. R. Sala, G. R. Stevenson and J. M. Zazula, Nucl. Instr. & Meth., **A332**, 459 (1993).

[11] C. Birattari, E. De Ponti, A. Esposito, A. Ferrari, M. Pelliccioni and M. Silari, Nucl. Instr. & Meth., **A338**, 534 (1994).

[12] C. Birattari, E. De Ponti, A. Esposito, A. Ferrari, M. Magugliani, M. Pelliccioni, T. Rancati, and M. Silari, *Measurements and simulations in high energy neutron fields*, Proc. of the 2nd "Specialists' Meeting on Shielding Aspects of Accelerators, Targets & Irradiation Facilities", CERN Geneva, October 12–13 1995, in press.

[13] P. R. Sala and A. Ferrari, Proc. of the MC93 Int. Conf. on Monte Carlo Simulation in High-Energy and Nuclear Physics, Feb. 22-26, 1993, Ed. P. Dragovitsch, S.L. Linn, M. Burbank, World Scientific, Singapore, 1994 (p. 277).

[14] Intermediate Energy Nuclear Data: Models and codes, Proc. of a Specialists' meeting, Issy-les-Moulineaux, May 30th - June 1st 1994, published by OECD/NEA (1994).

[15] F.W. Bopp et al., Phys. Rev. **D49** (1994) 3236; P. Aurenche et al., Phys. Rev. **D45** (1992) 92.

[16] G. Battistoni, A. Ferrari, and P.R. Sala, *Background calculations for the ATLAS detector and hall* Atlas internal note ATLAS-GEN-010, October 1994, and addendum, January 1995.

[17] A. Ferrari and P.R. Sala, *Background Rates in the Muon System: recent results and the Effect of the Tungsten plug*, Atlas internal note ATLAS-MUON-NO-090 (1995).

[18] M. Huhtinen and P.A. Aarnio, Nucl. Instr. Meth. **A335** (1993) 580.

[19] A.M. Ougouag et al., IEEE Trans. Nucl. Sci. **37** (1990) 2219.

[20] A. Ferrari, G. Battistoni and P.R. Sala, *Muon Chamber Sensitivity to neutron and photon background in the ATLAS hall*, Atlas internal note ATLAS-MUON-NO-052 (1994).

[21] A. Ferrari, K. Potter and S. Rollet, *Lateral Shielding Requirements for the ATLAS Experimental Region*, CERN Internal Report CERN/AT-XA/02N/95 (1995).

[22] A. V. Sannikov and E. N. Savitskaya, *Ambient Dose and Ambient Dose Equivalent Conversion Factors for High Energy Neutrons*, CERN Internal Report CERN/TIS-RP/93-14 (1993).

[23] R. Thomas and G. R. Stevenson, *Radiological Safety Aspects of the Operation of Proton Accelerators*, Technical Report Series No 283, IAEA Vienna (1988).

[24] G. R. Stevenson, A. Fassò, *A comparison of a MORSE calculation of attenuation in a concrete-lined duct with experimental data from the CERN SPS*, Proc. Topical Conference on Theory and Practices in Radiation Protection and Shielding, Knoxville 22-24 Apr. 1987, p. 428.

[25] A. Ferrari, K. Potter and S. Rollet, *Shielding for the ATLAS Experimental Region*, LHC Project Note 6 (1995).